

**Simulation of hard x-rays source produced by a picosecond laser
irradiated solid target for Compton radiography**

Meng-Ting, L.; Guang-Yue, H.; Huang, L.; Jian, Z.;

Originally published:

July 2020

Plasma Physics and Controlled Fusion 62(2020)095006

DOI: <https://doi.org/10.1088/1361-6587/ab9a60>

Perma-Link to Publication Repository of HZDR:

<https://www.hzdr.de/publications/Publ-31440>

Release of the secondary publication
on the basis of the German Copyright Law § 38 Section 4.

Simulations of Hard X-rays Source Produced by Picosecond Laser Irradiated Solid Target for Compton Radiography

Meng-ting Li¹, Guang-yue Hu^{*1, 2}, Lin-gen Huang^{**3}, Jian Zheng^{1, 4}

1 CAS Key Laboratory of Geospace Environment & Department of Engineering and Applied Physics, University of Science and Technology of China, Hefei, Anhui 230026, China

2 CAS Center for Excellence in Ultra-intense Laser Science(CEULS), Shanghai 200031, China

3 Helmholtz-Zentrum Dresden-Rossendorf (HZDR), Bautzner Landstraße 400, D-01328 Dresden, Germany

4 Collaborative Innovation Center of IFSA (CICIFSA), Shanghai Jiao Tong University, Shanghai 200240, China

*E-mail: gyhu@ustc.edu.cn

** E-mail: lingen.huang@hzdr.de

Abstract

Bremsstrahlung radiation hard x-ray source, produced by picosecond intense laser irradiated solid target, was used to diagnose implosion capsule at stagnation phase via Compton radiography in experiments. By performing Monte Carlo & Particle-in-Cell (PIC) simulation, we investigated the influence of target materials and laser intensity on the >70keV bremsstrahlung hard x-ray emission. We found that the brightness of the hard x-rays is proportional to the atomic number multiplied by area density ($Z\rho L$), which indicates that the higher Z and higher density gold or Uranium material will produce the brightest hard x-rays source at the same thickness. In relativistic laser solid interactions, hot electron recirculation plays an important role in the hard x-rays emission. Without recirculation, hard x-rays conversion efficiency decays when increasing the laser intensity. While the hard x-rays emission comes to the maximal saturated conversion efficiency at relativistic laser intensity if considering the electron recirculation. Those results provide valuable insights into the experimental design of Compton Radiography.

Keywords: inertial confined fusion, Compton radiography, numerical modeling

1. Introduction

In inertial confinement fusion (ICF) experiments, the imploded capsule has size of about $100\ \mu\text{m}$ and stays for about $150\ \text{ps}$ at stagnation phase during which fusion reaction occurred¹. It demands the diagnostic system with a spatial resolution of $10\ \mu\text{m}$ and temporal resolution of the order of $10\ \text{ps}$ to detect the capsule structure. Conventional nuclear diagnostic technologies cannot obtain such a high resolution. Thus, Compton radiography using hard x-rays source is a critical approach to diagnose the implosion target at stagnation phase.

Hot spot of implosion target will generate intense broadband bremsstrahlung x-rays self-emission, which can exceed the brightness of any other x-ray probe beams achieved at present. Fortunately, the warm hot spot plasma ($<10\text{keV}$) make the x-rays intensity decreases rapidly at hard x-ray range^{2,3}. Therefore, hard x-rays backlighting source above 70keV were used to resolve the capsule structure from intense x-rays background noise of self-emission in Compton radiography.

Short intense laser irradiated solid targets attract a lot of interest^{4,6}, which can generate bright picosecond hard x-rays source with tens of microns size for Compton Radiography. Laser driven $K\alpha$ emission was used as mono-energetic x-ray backlighter in some experiments of high energy density physics⁷⁻¹⁵. However, the conversion efficiency (CE) of $K\alpha$ x-rays source drops rapidly at hard x-rays range of $>20\text{keV}$ (typically $\text{CE}\sim 10^{-5}-10^{-4}$)⁹. At $>70\text{keV}$ hard x-rays range, bremsstrahlung continuum x-rays emission will be dominated⁵ (typically $\text{CE}\sim 10^{-4}-10^{-3}$). Moreover, according to Klein-Nishina formula¹⁶, the cross-section of Compton scattering is insensitive to the x-rays photon energy from several tens of keV to one hundred keV. The spectral response of detector is also non-sensitive to x-rays photon energy at this range. So, it is feasible to use the broadband bremsstrahlung hard x-rays emission between 70 and 200 keV as backlighter for Compton radiography.

Several experiments have been conducted at TITAN, OMEGA EP, and ARC laser facility to explore the hard x-rays source for Compton radiography^{4-6, 17, 18}. It show that the 75-100 keV bremsstrahlung hard x-rays emission depends on the target atomic number, and the laser intensity.

In the relativistic laser intensity, electron recirculation plays an important role in the hot electron motion produced by short pulse laser irradiated solid target. Part super-hot electrons escape away from the target, which lead to a sheath electrostatic field by charge separation at both sides of the target. Most of the remained hot electrons are trapped by the sheath field, recirculate many times between the front and rear side of the target, and are accelerated repeatedly by the laser field¹⁹. Electron recirculation increases the electron density and energy²⁰⁻²³, the sheath field and thus the proton acceleration²⁴, and $K\alpha$ x-rays emission^{19, 25-28} etc. It also causes isotropic x-rays emission²⁹ and enlarge the size of x-rays source³⁰.

In this paper, bremsstrahlung hard x-rays source of $>70\text{keV}$ emitted by picosecond laser irradiated solid targets was studied as a function of the target material, and laser intensity using Monte Carlo and PIC simulations. It's found that the CEs of $>70\text{keV}$ hard x-ray was proportional to the target's atomic number multiplied by density ($Z\rho L$), which provides a useful rule to quantitative analysis the x-rays brightness for experimental design. We found that the hard x-rays emission are sensitive to electron recirculation effect as that of the $K\alpha$ x-rays emission¹⁹, which produces increased CE of $>70\text{keV}$ hard x-ray emission in relativistic laser intensity, opposite to that without electron recirculation.

2. Simulation models

Monte Carlo and PIC codes were used in the simulation. PIC code was used to obtain the electron motion in laser-target interaction. Then the electron motion was import into the Monte Carlo code to calculate the x-rays emission. In the first part that explored the target materials and electron temperature dependence, only Monte Carlo code was used at which the

electrons experience a single trip through the target with given electrons kinetic energy. In the second part that investigated the electron recirculation effect, Monte Carlo code were coupled with the PIC code.

2.1 Monte Carlo model to calculate the x-rays emission

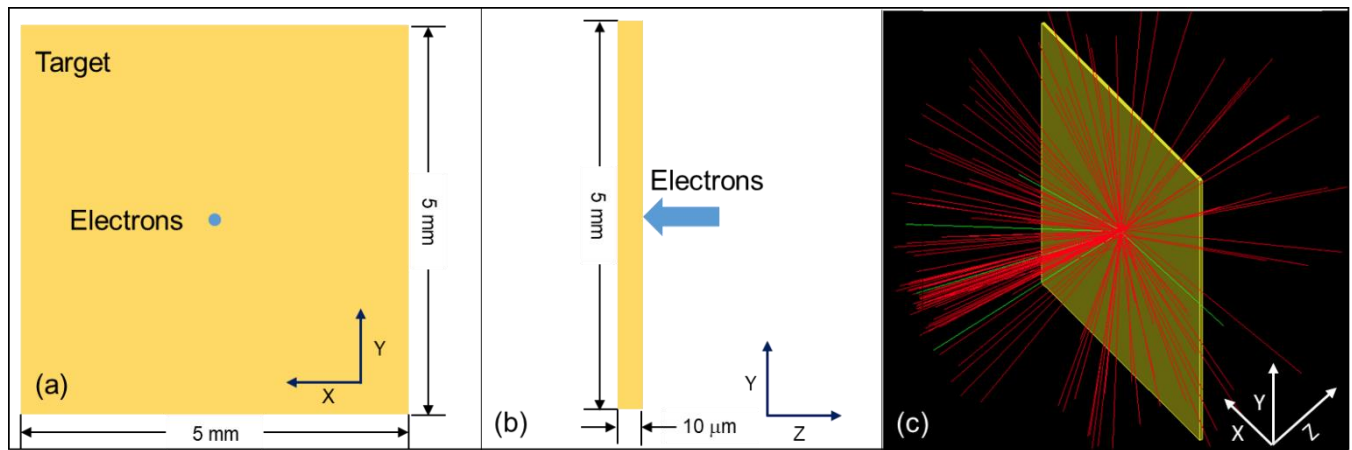


Fig. 1. Scheme of the Monte Carlo simulation using Geant4 code. (a) Front view from the direction of Z-axis. The yellow area represents the targets, and the blue dot represents position of the incident electrons. (b) Side view from the direction of X-axis. The blue arrow represents the direction of incident electrons. (c) A 3-D illustration of the target and the generation of secondary particles. The red lines represent the secondary electrons and green lines represent the photons.

The bremsstrahlung hard x-rays emission was calculated by Geant4 code³¹ based on Monte Carlo method. From the existing suite of physical packages, the “PhysListEmStandard” module was selected. It includes models for ionization, Bremsstrahlung, photoelectric effect, Compton scattering, and gamma conversion. The cross section of bremsstrahlung emission is based on the interpolation of the data from public tables^{32,33}. The capability of Geant4 to simulate the particle induced x-ray emission has been validated by comparing the simulations with measured spectrum³⁴⁻³⁶.

Fig. 1 depicts the scheme of the Monte Carlo simulation for energetic electrons hit the target and produce x-rays. The target has 5 mm × 5 mm transvers size and 10 μm thickness. Incident electrons shoot at the center of the front surface, shown as the blue spot in Fig. 1(a), and enter the target along the normal direction (z-axis). Fig. 1(c) is the 3D illustration of a simulation. The red lines represent the outgoing secondary electrons and green lines represent the photons.

Since the codes cannot deal with the laser absorption and hot electrons generation, some assumption was required to describe the kinetic energy distribution of the incident electrons. Usually, we set the incident electrons with normalized energy distribution functions (EDF), such as Boltzmann distribution³⁷⁻³⁹, $f(E) \propto \exp(-E/T_h)$, Maxwell distribution⁴⁰, $f(E) \propto E^{1/2} \exp(-E/T_h)$, and relativistic Maxwell distribution^{41,42}, $f(E) \propto E^2 \exp(-E/T_h)$, where E is the kinetic energy of electrons and T_h is the electron temperature decided by the laser intensity in experiments. 10^8 electrons were shooting in each case of simulation. All the incident electrons either experience a single trip through the target before escaping, or lose all

the energy and merge in the target before reaching the backside. X-ray photons outgoing in 4π solid angles carrying energy within a specific energy band ($k1 \sim k2$) were counted to calculate the energy conversion efficiency from electron into the x-rays ($\eta_{e \rightarrow X}^{k1 \sim k2}$).

2.2 2D-PIC models to calculate the hot electrons generation

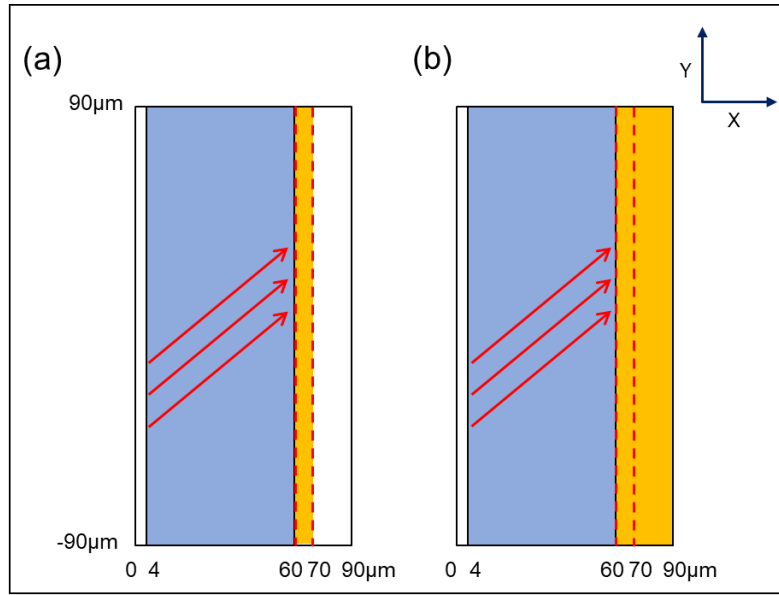


Fig. 2. Scheme of the 2D-PIC simulation. The yellow region presents the gold target. The blue region presents the preplasmas in front of the target. The red arrows indicate the direction of the incident laser. The white area presents the vacuum. The red dash lines are boundary of probe box to count the direction of motion and energy distribution of hot electrons. (a) A 10 μm thin foil considering electron recirculation effect. (b) A thick target to inhibit electron recirculation effect whose rear surface attaching to the boundary of the simulation area at $x=90\mu m$.

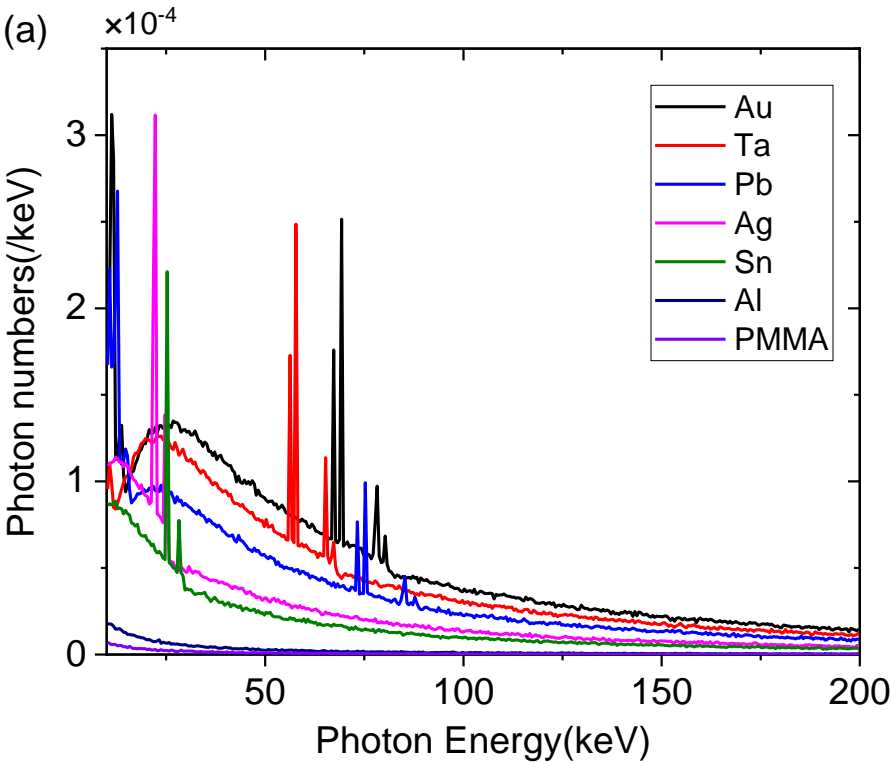
Hot electrons generated in the interaction of laser-target is simulated using 2D PIC code - PICLS⁴³ in the (X, Y) plane. In the simulations, we set laser energy $E_{laser}=30J$, laser wavelength $\lambda=1\mu m$. Both of the temporal and radial laser profiles are Gaussian distribution, with full width half maximum (FWHM) duration $\Delta t_{FWHM}^{laser}=0.6 ps$, and FWHM spot size $\Phi_{FWHM}^{laser}=30\mu m$, which gives the peak laser intensity $4.4 \times 10^{18} W/cm^2$. Laser beam is p-polarized and incident at 45° with respect to the target normal. The cell size is $\Delta x=\Delta y=1/40\mu m$ with 5 macroparticles per cell. The ions are fixed. Boundary conditions for the fields are periodic at the transverse boundaries ($y=-90\mu m, 90\mu m$) and absorbing at the longitudinal boundaries ($x=0, 90\mu m$, while for the particles are thermal reflecting in order to keep the total charge equal to zero. The total simulation time is 2 ps. As showed in Fig. 2, the yellow region presents the gold target with the density equaling to $5n_c$, where $n_c = 1.1 \times 10^{21} cm^{-3}$ is the critical density of the laser pulse. Here the reduced density is used to save the computational time. The blue region presents the preplasmas in front of the target. The density profile of preplasmas is set as $N_e(x) = 5n_c \exp(-(x-60)/L_p)$, where $L_p =$

$6\mu m$ is the preplasma scale length and $x=60\mu m$ is the position of main target's front surface. The white area presents the vacuum. Fig. 2(a) is the case of a $10\mu m$ thin foil target, at which electron recirculation is significant due to the sheath fields. Fig. 2(b) is the case of thick target that electron recirculation do not occurs. In this case, the target rear surface is attached to the boundary of the simulation area at $x=90\mu m$, at which hot electrons are thermally reflected (equivalent to absorbed) by the rear boundary. The red dash lines marked the probe box with $10\mu m$ width that diagnoses the motion of hot electrons. When an electron with energy more than 50 keV escapes from the probe box, it will be taken into account to calculate the energy and angular distribution of hot electrons. The energy and angular distributions of hot electrons from PIC simulations are then coupled to the Monte Carlo code to calculate the x-rays emission. We notice the atomic ionization processes are neglected in our PIC simulations to save the computational time and simply the physics. It is worthy to perform more realistic numerical simulations by including the ionization physics in the future work.

3. Monte Carlo simulation results

In this part, the hot electrons experience a single trip when transporting the target (without electron recirculation effect) using Monte Carlo simulation to explore the influence of target materials and electron temperature/ laser intensity on hard x-rays emission.

3.1 Influence of target materials on hard x-rays emission (without electron recirculation)



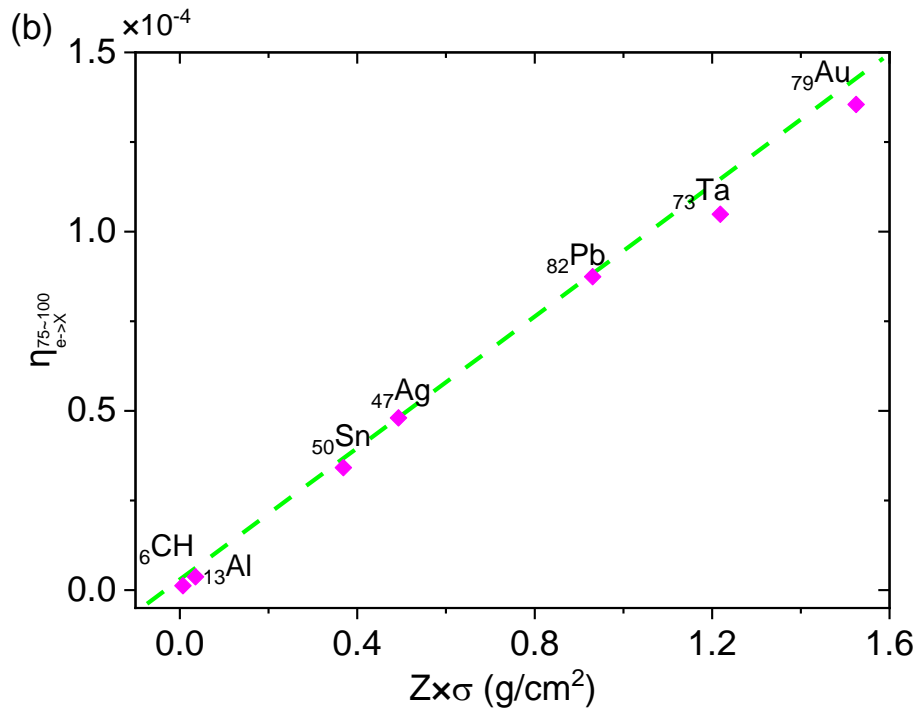


Fig. 3. (a) Angularly integrated hard x-rays spectra (10~200 keV) emitted by Au, Ta, Pb, Ag, Sn, Al and PMMA (CH) materials with 10 μ m thickness. The number of photons is normalized to a single incident electron. (b) The conversion efficiency from electron energy into x-rays emission of 75-100keV x-rays ($\eta_{e \rightarrow X}^{75 \sim 100}$) versus $Z\rho L$. Z represents the atomic number of material and ρL represents the area density. The green dash line shows a proportionality relationship between them.

In this section, we presumed that the incident electrons follow the Maxwell distribution with temperature of 500 keV corresponding to the laser intensity of 9×10^{18} W/cm² according to Beg' scaling law⁴⁴, i.e. $f(E) \propto E^{1/2} \exp(-E/T_h)$, where E is the kinetic energy of electrons in unit of keV. Seven materials were used in simulation. Fig. 2(a) plots the angularly integrated x-rays energy spectra in the range of 10~200 keV. The number of photons was normalized to a single incident electron. It can be clearly seen that K_α and K_β characteristic lines stand above the continuum emission substrate except for PMMA (CH) and Al. For Ta, Au and Pb, the L -band line emissions are also well defined besides the K -band lines. The characteristic lines emission of Au and Pb fall within the scope of 75 ~ 100keV we are interested in. For all of the curves, the number of photons gradually increases from high energy to low energy x-rays, reaching a peak, and further decreases due to the reabsorption of the material.

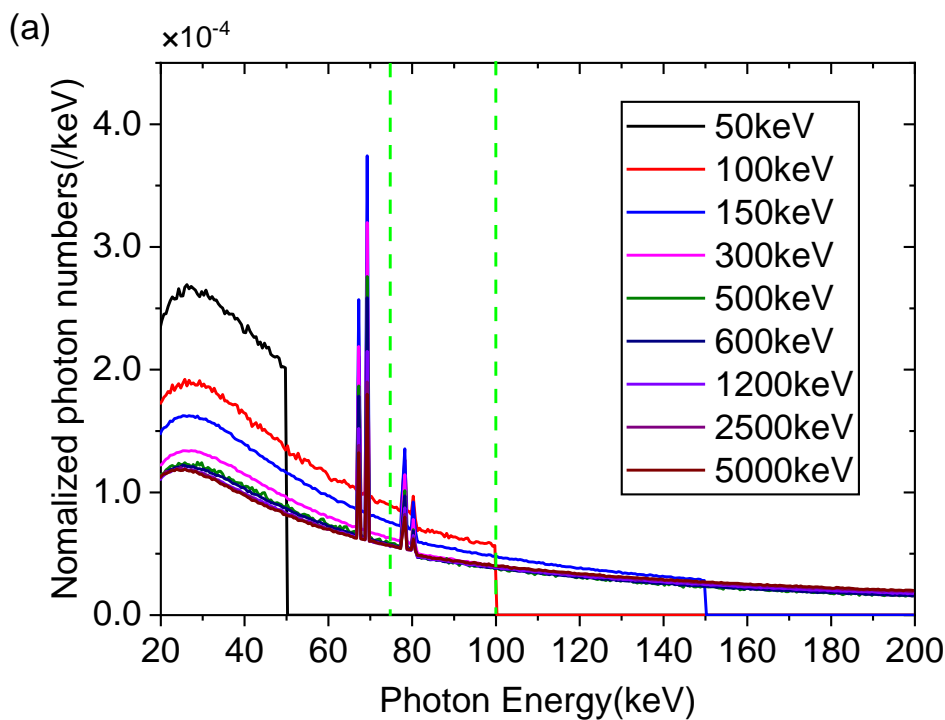
Figure 3(b) plots the conversion efficiency from electron energy into x-rays emission of 75~100 keV (i.e. $\eta_{e \rightarrow X}^{75 \sim 100}$) versus $Z\rho L$, in which Z represents the atomic number of material and ρL represents the area density (ρ is the density, L is the thickness). It indicates that $\eta_{e \rightarrow X}^{75 \sim 100}$ is proportional to $Z\rho L$. The observation is similar to the experimental result from LLNL⁵ which shows CEs increasing with the mass density. The proportionality can be inferred from the differential cross-section⁴⁵ of bremsstrahlung radiation which is proportional to the square of the atomic number Z^2 , leading the total probability of bremsstrahlung proportional to $Z^2 \times n$, in which n presents the number of atoms in the path of the electron. That is, the

intensity of the bremsstrahlung is proportional to $Z\rho L$. The conclusion is true only if the reabsorption can be neglected, which is always satisfied under the condition of hard x-rays of tens of keV passing through the targets of several micrometers.

According to this rule, material of high Z and high density such as Au or Uranium should be used as target material in laser-driven backlighter^{17, 18, 46-48}. In contrast, low- Z and density material such as CH is the ideal substrate material, which gives no discernible background noise in 2D Compton Radiography experiments⁶.

From the simulation results, all of the material have the $\eta_{e \rightarrow X}^{75 \sim 100}$ of 10^{-5} to 10^{-4} in 75~100 keV x-rays range. If we assume that the laser absorption is 0.4 at the corresponding laser intensity⁴⁹, the conversion efficiency from laser energy into x-rays of 75~100 keV ($CE_{75 \sim 100}$) has a maximum about 5.4×10^{-5} for Au. The $CE_{75 \sim 100}$ is far lower than the experimental result⁵ of about 10^{-3} . The discrepancy should be caused by electron recirculation effect that we did not consider here, which will be discussed in Sec. 4.

3.2 Dependence of X-rays emission on laser intensities/ electron temperature (without electron recirculation)



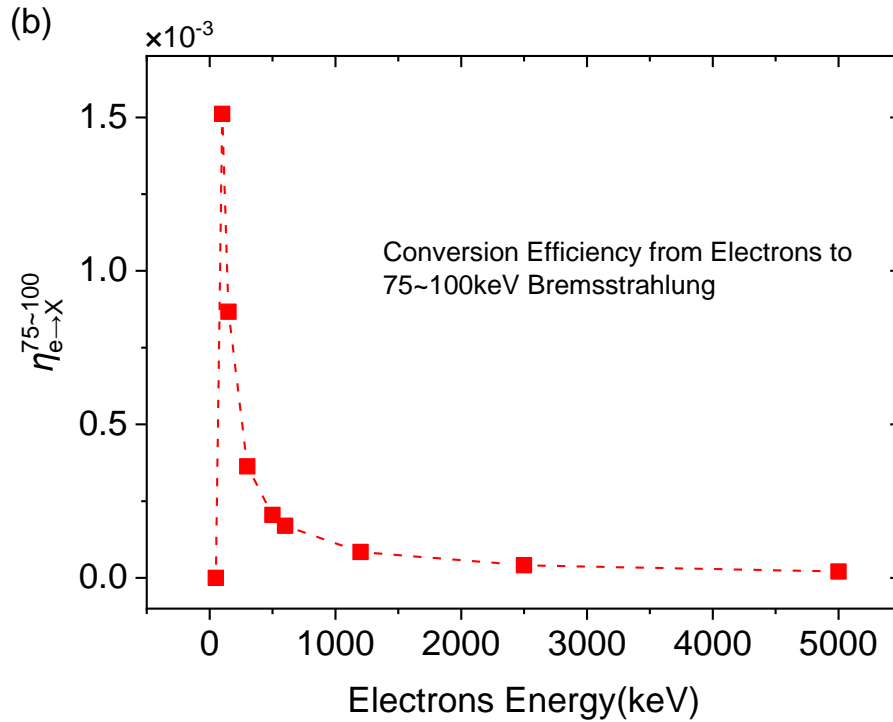


Fig. 4. (a) Angularly integrated x-rays spectra from 10 μ m gold foil driven by mono-energetic incident electrons. The green dash lines enclose the scope of 75~100 keV in which x-ray photons are used to calculate CE. The number of photons is normalized to a single incident electron. (b) The CE versus the kinetic energy of mono-energetic incident electrons.

To analyze the quantitative characteristics of hard X-rays emission under various type of electrons distribution function (EDF), mono-energetic electrons of different energy as incident particles were studied firstly. Fig. 4(a) showed the angularly integrated x-rays energy spectra from 10 μ m gold foil in the range of 20~200 keV driven by mono-energetic incident electrons with 50 keV- 5 MeV kinetic energy. The number of photons is normalized to a single incident electron. It can be found that, mono-energetic electron beam can only produce x-ray with energy lower than that of the incident electrons. For all the energies of incident electrons, continuum x-ray emission decreases exponentially with photon energy increasing above 30 keV. The green dash lines enclose the scope of 75~100keV which we are interested in. It is notable that the characteristic lines emissions of Au fall within this scope. The number of photons in this scope decrease with the increasing kinetic energy of the incident electrons. It's because the x-rays emission is getting broader spectrum at higher electron energy, thus more energy is converted to higher energy photons beyond 100keV. Fig. 4(b) gives the $\eta_{e \rightarrow X}^{75 \sim 100}$ versus kinetic energy of the mono-energy incident electrons. The CE value is 1.5×10^{-3} at 100 keV, but falls sharply to 2×10^{-4} at 500 keV, and continuously decays slowly at higher incident electron energy. Therefore, the electrons around 100 keV produce more x-rays emission of 75~100 keV than other electron kinetic energy.

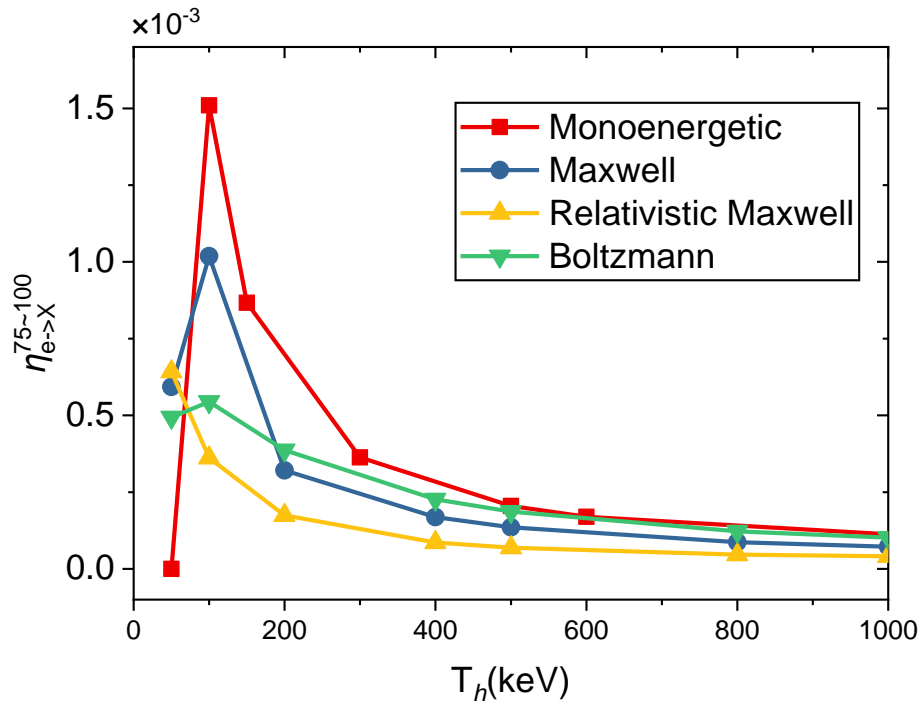


Fig. 5. The 75-100keV x-rays $\eta_{e \rightarrow X}^{75 \sim 100}$ emitted by 10 μ m gold foil versus the temperature of incident electrons (T_h) which following different electron distribution function (EDF).

Fig. 5 demonstrates the $\eta_{e \rightarrow X}^{75 \sim 100}$ of 75-100keV x-ray emission versus the temperature of electrons (T_h), following different type of EDF: Boltzmann distribution, Maxwell distribution, relativistic Maxwell distribution, and Mono-energetic distribution. Since the electron energy is distributed over a large energy range at given EDF, even if the electron temperature is lower than 75 keV, x-rays of 75 to 100 keV can still be generated. The highest $\eta_{e \rightarrow X}^{75 \sim 100}$ obtained near the electron temperature of 100 keV. When the electron temperature is lower ($T_h < 75$ keV), most of the hot electrons are below 75 keV and cannot produce x-rays of 75-100 keV. At higher electron temperatures ($T_h > 100$ keV), a large amount of electron carry energy higher than 100 keV and also cannot effectively generate x-rays of 75-100 keV. The maximal $\eta_{e \rightarrow X}^{75 \sim 100}$ is around 10^{-3} at the temperature of 100 keV for Maxwell distribution, which is lower than the $\eta_{e \rightarrow X}^{75 \sim 100}$ of 1.5×10^{-3} at mono-energetic incident electrons case. When the temperature (or kinetic energy) of energetic electrons is above 200 keV, the CE relationship is that Mono-energetic > Boltzmann distribution > Maxwell distribution > Relativistic Maxwell distribution, although the difference between them is very slight.

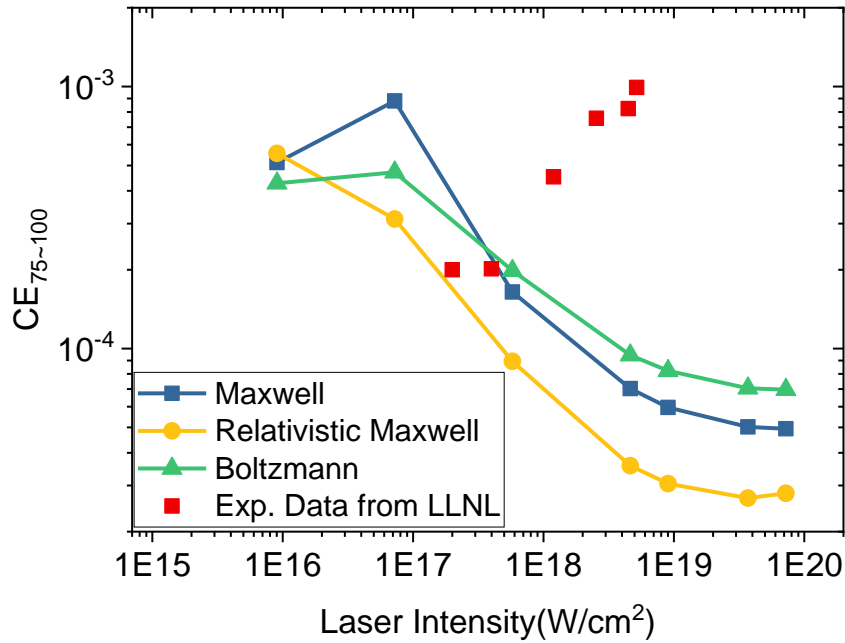


Fig. 6. The x-rays CE emitted by 10 μ m gold foil from laser energy to 75-100keV x-rays emission ($CE_{75\sim 100}$) versus the laser intensity. MC simulation results without electron recirculation (color lines), and the experimental data (red squares) inferred from Ref.⁵ in which 25 μ m thick Au (at 2×10^{17} W/cm²) foil and 10 μ m thick Au ($>5\times 10^{17}$ W/cm²) were presented. The laser absorption ratios were taken from Ref.⁴⁹

Fig. 6 shows the dependence of the CEs from laser energy into x-rays of 75~100 keV (i.e. $CE_{75\sim 100}$) on the laser intensity, which calculated by using the data in Fig. 5. The conversion efficiency is calculated by $CE_{75\sim 100} = \eta_{e\rightarrow X}^{75\sim 100} \times \eta_{abs}$, in which η_{abs} is the laser absorption ratio determined by the experimental and simulation data from Ref.⁴⁹ which depends on laser intensity. The electron temperature at corresponding laser intensity is calculated by using Beg's scaling law⁴⁴. Boltzmann distribution, Maxwell distribution and Relativistic Maxwell distribution are displayed, along with the data of experiments⁵ conducted on TITAN for comparison. When laser intensity is in the nonrelativistic region (about 5×10^{17} W/cm²), the simulation result is in good agreement with the experimental data. The $CE_{75\sim 100}$ is about 2×10^{-4} for both of them. When laser intensity exceeds 1×10^{18} W/cm² which reach the relativistic region, the simulation result decreases with the laser intensity, and finally reaches a value about 5×10^{-5} for Maxwell distribution. However, the experimental results present an opposite trend, which shows the CE increases with the laser intensity getting higher. When laser intensity is closer to 10^{19} W/cm², the experimentally obtained $CE_{75\sim 100}$ is about 10^{-3} , which is two orders higher than the simulation results. The discrepancy indicates that at relativistic laser intensity, the Monte Carlo simulations without electron recirculation are incapable of calculating the x-ray emission. A precise understanding of the electron generation and transport in the target is requested, which will be shown in the following section of PIC+Monte Carlo simulation.

4. PIC & Monte Carlo simulation results with electrons recirculation

4.1 Electrons energy distribution given by PIC simulation

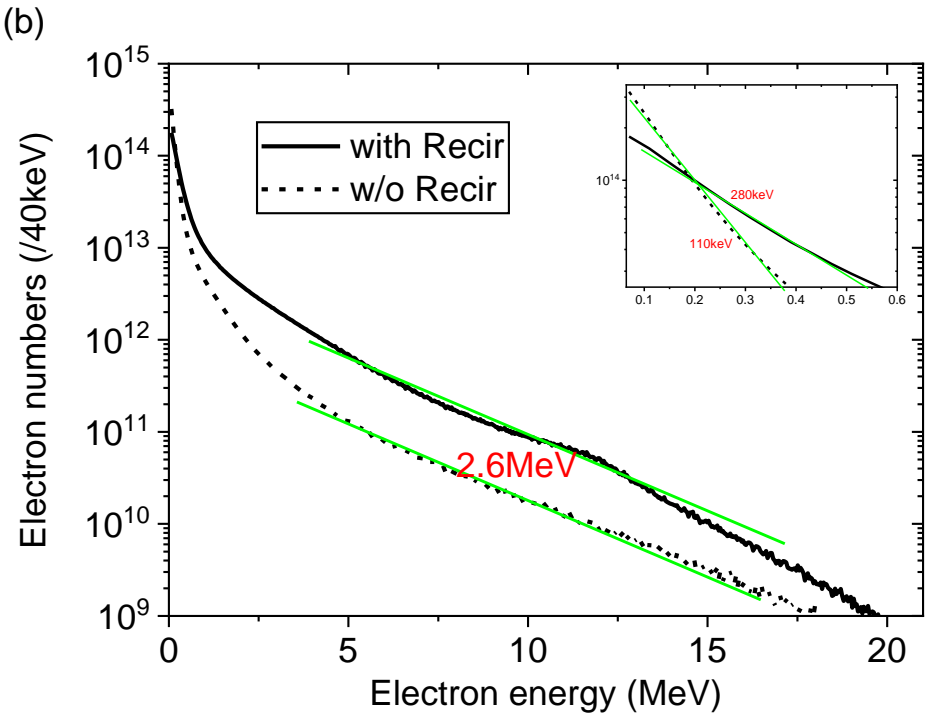
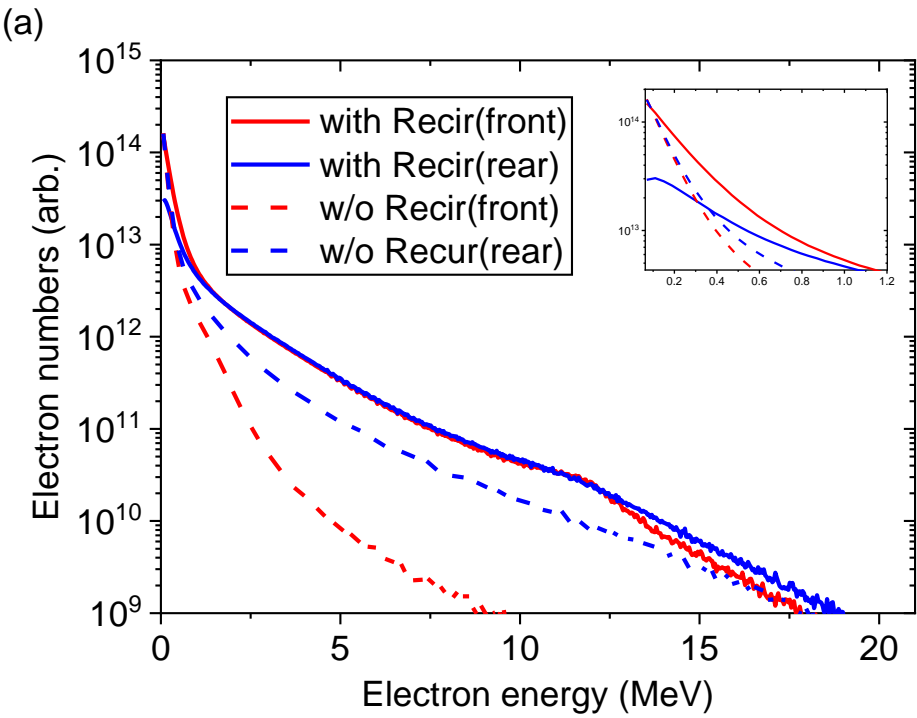


Fig. 7. Electron energy distribution (>70 keV) counted at both sides of the probe box in PIC simulation with (solid lines) or without (dash lines) electron recirculation effect. (a) Results counted at each side of the probe box, (b) results that sum both sides of the probe box. The insert shows the enlarged view of the low-energy range

The electrons energy distribution from 70 keV to 20 MeV counted at both side of probe box in PIC simulation are presented in Fig. 7(a). In the case of thick target without electron recirculation, the number of electrons emitted from the front side is less than that from the rear side, especially in the higher energy range. It is because most of the electrons are accelerated forward by laser ponderomotive force. In contrast, for the thin foil case including electron recirculation, the number of electrons emitted from the front side is comparable to that from the rear side in the spectral range higher than 1 MeV, which means isotropic electron motion. It indicates the formation of the sheath electrostatic field at the rear surface of the thin foil. The sheath field at rear side restricts electrons escape, while the preplasmas at the front side destroys the sheath field and permits electrons escape. Therefore the number of low-energy electrons (<200 keV) counted at the rear side of thin foil is smaller than that at the front side. The scenario can be clearly seen from the spatial distribution of the electrostatic field, as shown in Fig. 8. In our specific case, the maximum sheath electrostatic field at rear surface is ~ 3.25 TV/m, while the sheath field at the front side is not so visible. The strong electrostatic sheath field at rear traps most energetic electrons and only a small fraction of them is able to escape to the vacuum, as also studied in our previous work⁵⁰.

The most significant change is that the electrons energy and number above 200 keV with electron recirculation are obviously higher than that without electron recirculation, as can be found in the sum energy distribution in Fig. 7(b). At 3-12 MeV, the electrons number is 8 times enhanced. Electrons recirculation mainly affects lower and middle energy electrons that can be reflected by sheath field. At highest electron energy close to 20 MeV, electron recirculation has no observed effect on electrons number. The EDF exhibits double temperature components. The high energy tail has a temperature of 2.6 MeV for both cases, and the lower-energy part have a temperature of about 228 keV for thin foil and 110 keV for thick foil.

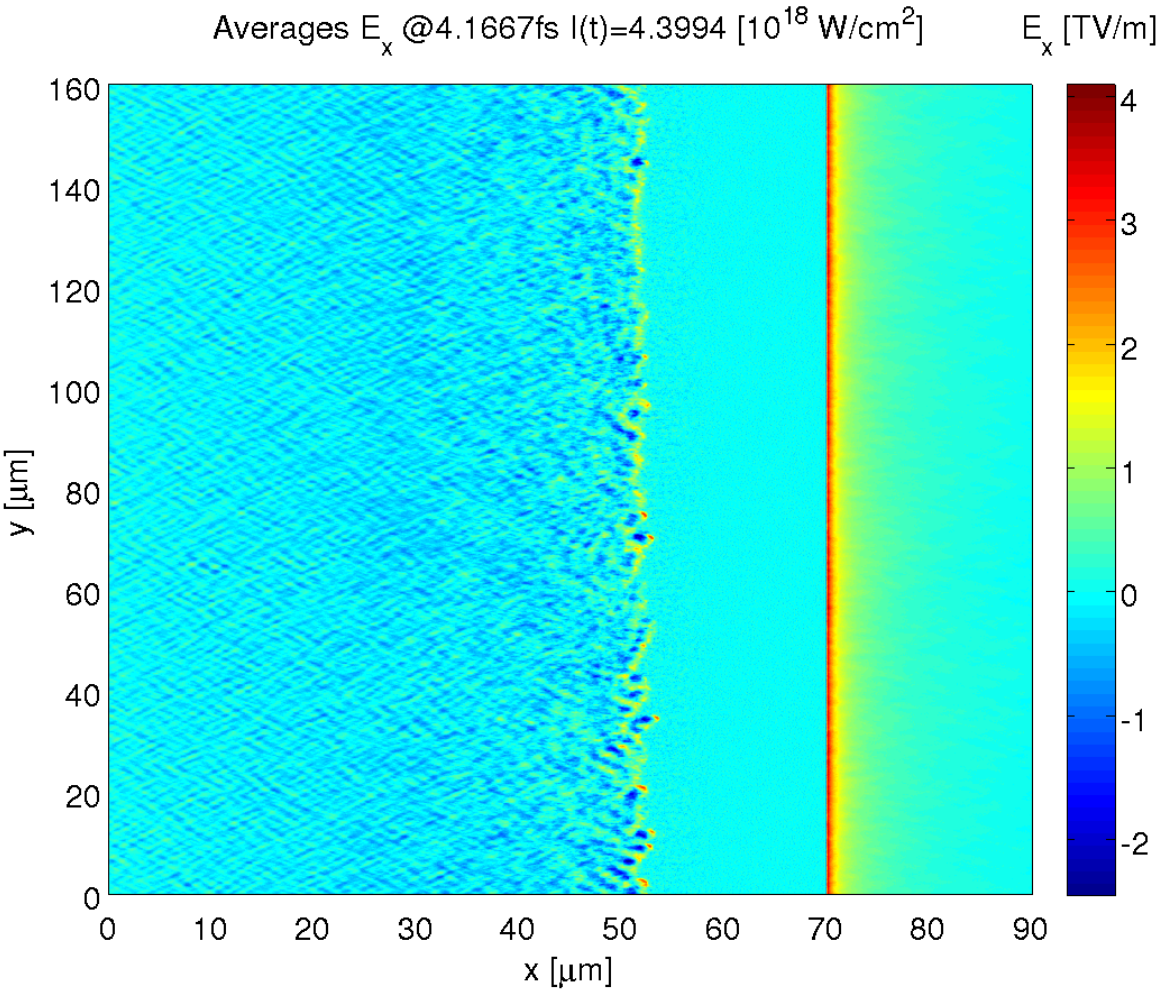


Fig. 8. The spatial distribution of the electrostatic field in the case of thin target with electron recirculation at ~ 4 fs after the laser peak intensity hitting the target.

4.2 X-rays emission spectra calculated by PIC+Monte Carlo

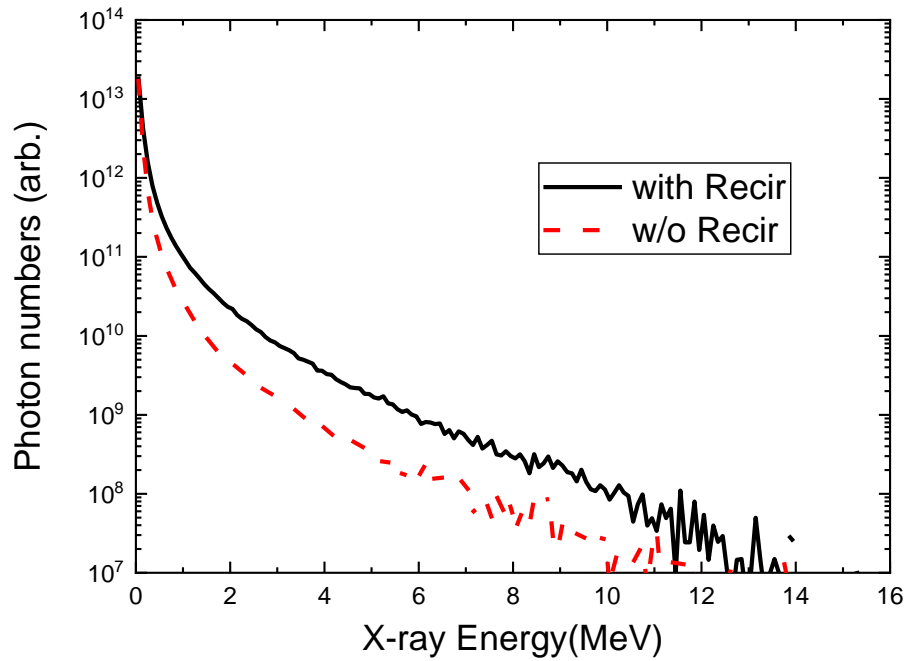
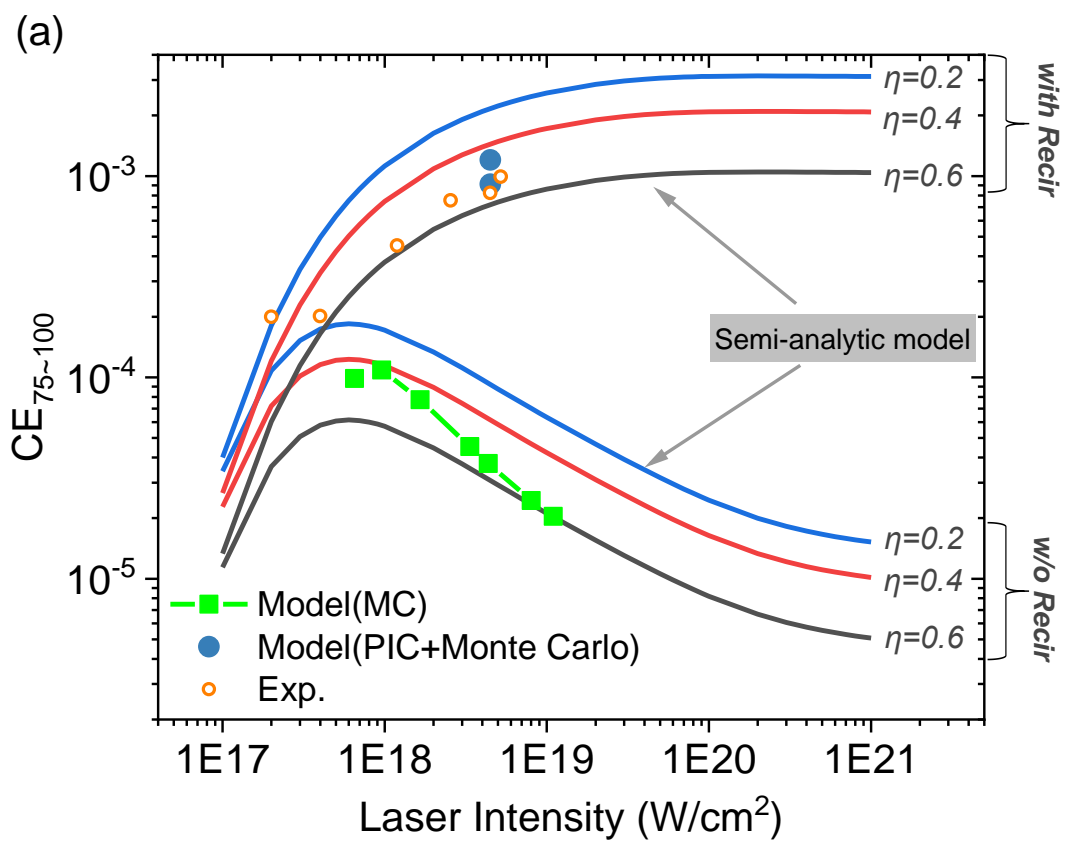
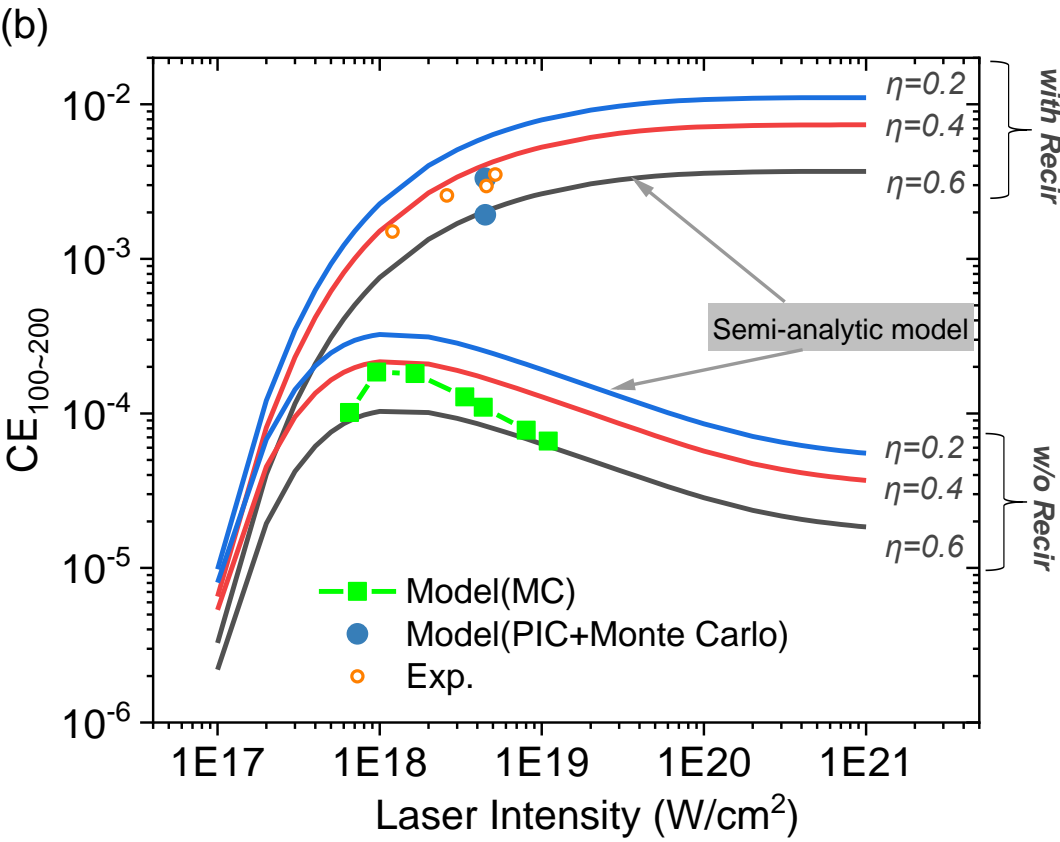


Fig. 9. Angularly integrated x-rays spectra emitted by 10 μ m Au foil with and without electron recirculation.

Electrons energy and angular distributions obtained from PIC code are input into the Monte Carlo code to calculate the x-rays emission from a 10 μ m Au foil. The angularly integrated x-ray spectra in 4π solid angles with and without electron recirculation are shown in Fig. 9. As expected, x-rays spectra have two temperature components. The x-rays intensity with electron recirculation is much higher than that without electron recirculation, but the difference in the low-energy range becomes smaller. At 5MeV, the x-rays are 10 times amplified by electron recirculation. While at 75-100keV, 100-200keV, and 70-200keV, the x-rays are only enhanced by 1.3, 1.7 and 1.6 times respectively, which is close to the experimental value of 1.7 for measured dose of x-rays from 50 keV to 80 MeV²².

4.3 Semi-analytic model of electron recirculation





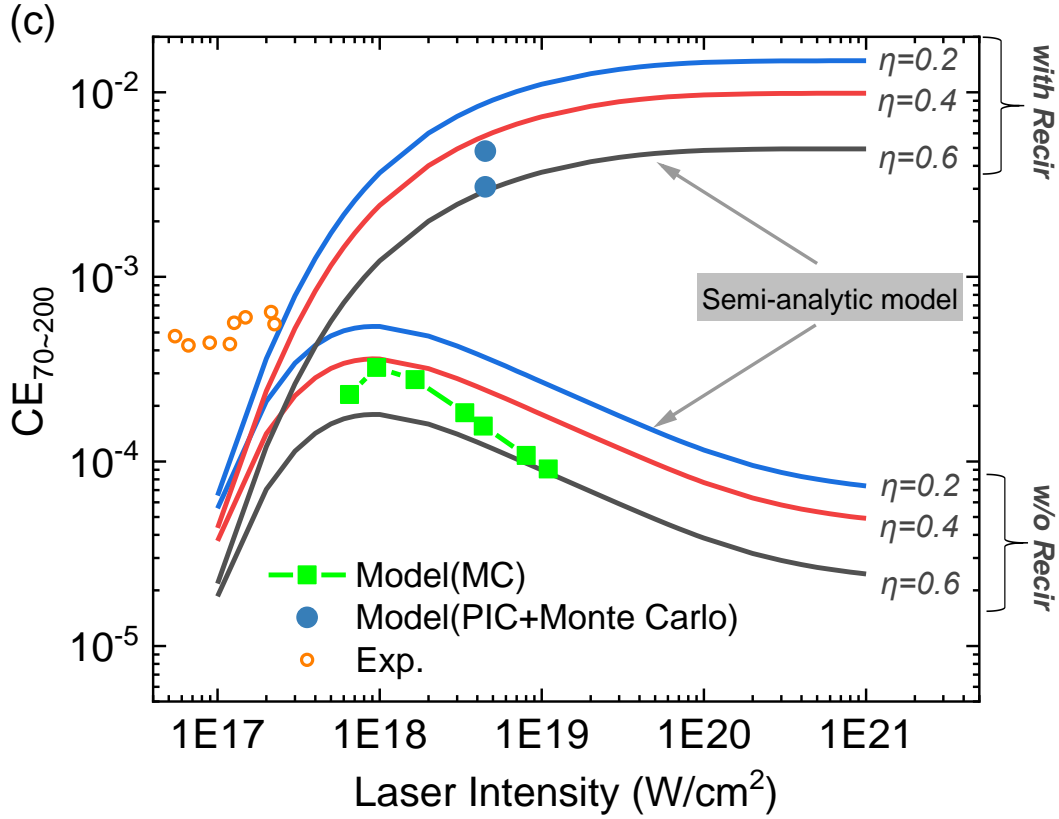


Fig. 10. Conversion efficiency from laser energy to hard x-rays emission of $10\mu m$ Au foil in the range of 75-100keV (a, CE_{75-100}), 100-200keV (b, $CE_{100-200}$), and 70-200keV (c, CE_{70-200}) with and without electron recirculation. In the curves of semi-analytic model (solid lines), the laser absorption ratio η_{abs} is set to 0.2, 0.4, and 0.6 respectively. PIC+Monte Carlo simulation results (blue dots, PIC+Monte Carlo), Monte Carlo simulation results using Boltzmann distributed incident electrons (green squares, MC), and experimental results (orange circles, Exp.) are also displayed.

We employ a semi-analytic model as discussed in Ref.¹⁹ to explore the influence of electron recirculation on the hard x-rays emission. A group of electrons following the Boltzmann distribution $f(E_0) = A \exp(-E_0/T)$ are injected into 10 μm Au foil from the front surface, where T is the temperature of the electrons determined by laser intensity⁵⁰: $T = 511 \times [\sqrt{(1 + I_{18} \lambda_{\mu\text{m}}^2)/1.37}] \text{keV}$, where I_{18} is the laser intensity in the unit of 10^{18}W/cm^2 . The total energy of the electrons is $E_{\text{electron}} = E_{\text{laser}} \times \eta_{\text{abs}} = \int_0^\infty f(E_0) dE_0$, where E_{laser} is the laser energy. Bremsstrahlung hard x-rays photons are emitted when the electrons propagate in the target. The total energy of bremsstrahlung photons from k_1 to k_2 generated in the target is calculated by

$$E_X = n_{\text{Au}} \int_0^\infty dE_0 f(E_0) \int_{k_1}^{k_2} k dk \int_0^s \sigma_k^{\text{brem}} [E(E_0, s'), k] ds' \quad (1)$$

where n_{Au} is the ion number density of Au equaling to $5.9 \times 10^{24} \text{cm}^{-3}$. k is the energy of emitted bremsstrahlung photons. The differential cross section of bremsstrahlung σ_k^{brem} is a function of the kinetic energy of scattered electron E and the radiated photon energy k . The integration variable s' is the path that an electron goes through in the target, and the up-limit s is the path length of an electron with primary energy of E_0 . The stopping power dE/ds' accounting for the energy loss of electrons in the target is obtained from the ESTAR stopping tables⁵¹.

In the case considering electron recirculation, all the hot electrons are assumed to be reflected between the front and rear surfaces of gold foil. They interact with the material until the energy is exhausted in the target volume, as if they are propagating in an infinite medium. So, the path length s is the maximum distance an electron can take in the material. It is a function of the initial energy of the electron $s = s(E_0)$.

In the case without electron recirculation, any electron will be discarded once it reaches the target's rear surface for the first time, or it is absorbed in the target before it arriving the rear surface. So, the path length s can't exceed the target thickness of 10 μm . It should be replaced by $\min[d, s(E_0)]$ in Eq. (1).

The calculated CE of hard x-rays emission in the range of 75-100keV, 100-200keV, and 70-200keV by the semi-analytic model are presented in Fig. 10. The laser absorptivity is set as $\eta_{\text{abs}} = 0.2, 0.4$, and 0.6 . For comparison, it also displayed the experimental results^{5, 18}, the CEs calculated by PIC+Monte Carlo method (from Fig. 9), and the Monte Carlo simulation results using Boltzmann distributed incident electrons (Fig. 6, η_{abs} is set to 0.2).

Without electron recirculation, the CEs increase to the peak value at about $1 \times 10^{18} \text{W/cm}^2$ and decline in the relativistic intensities. The curve profiles given by the semi-analytic model are consistent with the results given by MC simulation since the electrons in both methods experience just a single trip across the target.

If considering electron recirculation, the semi-analytic model predicted CEs increase rapidly with the laser intensity from 10^{17}W/cm^2 to 10^{18}W/cm^2 and almost saturate over the range from 10^{18}W/cm^2 to 10^{21}W/cm^2 . Both of the results given by semi-analytic model with electron recirculation and the PIC+Monte Carlo simulation are in good agreement with the experimental results, which are one order higher than that without electron recirculation.

At nonrelativistic laser intensity of $< 1 \times 10^{18} \text{W/cm}^2$, there is no obvious difference between that with or without electron recirculation. Both of them reproduced the measured CE_{75-100} and CE_{70-200} at $2 \times 10^{17} \text{W/cm}^2$ (see Fig. 10(a) and (c)), at which the electrons energy is so low that most of them have a stopping range shorter than the target thickness. Thus, the electron recirculation doesn't work in nonrelativistic laser intensity. The model underestimates the CE_{70-200} in the lower-intensity region. It may be caused by the improper electron temperature estimation in the non-relativistic laser intensity using the pondermotive scaling law.

5. Conclusion

Target materials and laser intensity dependence of $>70\text{keV}$ bremsstrahlung hard x-rays emitted by picosecond laser irradiated solid target were investigated by using PIC and Monte Carlo simulation. It's shown that the hard x-rays brightness is proportional to the product of target's atomic number Z and area density ($Z\rho L$). Thus, high Z and high density material of gold or Uranium should be chosen as illuminant target, and low Z material of CH can be used as substrate in experiments of Compton radiography. We found that electron recirculation plays an important role in the generation of hard x-rays at relativistic laser intensity, while it can be ignored at nonrelativistic laser intensity. It enhances the hard x-rays emission markedly and produces the brightest saturated x-rays emission at laser intensity over the range from 10^{18}W/cm^2 to 10^{21}W/cm^2 , which place greater demands on laser intensity for Compton radiography.

Acknowledgement

This work was supported by the Strategic Priority Research Program of Chinese Academy of Sciences (Grant No.XDB16000000), the National Natural Science Foundation of China (Grant Nos. 11775223, 11375197, 11605200, and 11275202), the Science Challenge Project (Grant No. TZ2016005), the Open Fund of the State Key Laboratory of High Field Laser Physics (SIOM), and the Fundamental Research Funds for the Central Universities.

Reference

[1] S. Atzeni and J. Meyer-ter-Vehn, The Physics of Inertial Fusion: BeamPlasma Interaction, Hydrodynamics, Hot Dense Matter. (Oxford University Press on Demand, 2004).

[2] J. F. Hansen, S. G. Glendinning, R. F. Heeter and S. J. Brockington, Rev Sci Instrum **79** (1), 013504 (2008).

[3] B. R. Maddox, H. S. Park, B. A. Remington, C. Chen, S. Chen, S. T. Prisbrey, A. Comley, C. A. Back, C. Szabo, J. F. Seely, U. Feldman, L. T. Hudson, S. Seltzer, M. J. Haugh and Z. Ali, Physics of Plasmas **18** (5), 056709 (2011).

[4] R. Tommasini, H.-S. Park, P. Patel, B. Maddox, S. Le Pape, S. P. Hatchett, B. A. Remington, M. H. Key, N. Izumi, M. Tabak, J. A. Koch, O. L. Landen, D. Hey, A. MacKinnon, J. Seely, G. Holland, L. Hudson and C. Szabo, in AIP Conference Proceedings (2007), pp. 248-258.

[5] R. Tommasini, A. MacPhee, D. Hey, T. Ma, C. Chen, N. Izumi, W. Unites, A. MacKinnon, S. P. Hatchett, B. A. Remington, H. S. Park, P. Springer, J. A. Koch, O. L. Landen, J. Seely, G. Holland and L. Hudson, Rev Sci Instrum **79** (10), 10E901 (2008).

[6] R. Tommasini, S. P. Hatchett, D. S. Hey, C. Iglesias, N. Izumi, J. A. Koch, O. L. Landen, A. J. MacKinnon, C. Sorce, J. A. Delettrez, V. Y. Glebov, T. C. Sangster and C. Stoeckl, Physics of Plasmas **18** (5), 056309 (2011).

[7] L. M. Chen, P. Forget, S. Fourmaux, J. C. Kieffer, A. Krol, C. C. Chamberlain, B. X. Hou, J. Nees and G. Mourou, Physics of Plasmas **11** (9), 4439-4445 (2004).

[8] H. S. Park, D. M. Chambers, H. K. Chung, R. J. Clarke, R. Eagleton, E. Giraldez, T. Goldsack, R. Heathcote, N. Izumi, M. H. Key, J. A. King, J. A. Koch, O. L. Landen, A. Nikroo, P. K. Patel, D. F. Price, B. A. Remington, H. F. Robey, R. A. Snavely, D. A. Steinman, R. B. Stephens, C. Stoeckl, M. Storm, M. Tabak, W. Theobald, R. P. J. Town, J. E. Wickersham and B. B. Zhang, Physics of Plasmas **13** (5), 056309 (2006).

-
- [9] H. S. Park, B. R. Maddox, E. Giraldez, S. P. Hatchett, L. T. Hudson, N. Izumi, M. H. Key, S. Le Pape, A. J. MacKinnon, A. G. MacPhee, P. K. Patel, T. W. Phillips, B. A. Remington, J. F. Seely, R. Tommasini, R. Town, J. Workman and E. Brambrink, *Physics of Plasmas* **15** (7), 072705 (2008).
- [10] E. Brambrink, H. G. Wei, B. Barbreil, P. Audebert, A. Benuzzi-Mounaix, T. Boehly, T. Endo, C. Gregory, T. Kimura, R. Kodama, N. Ozaki, H. S. Park, M. R. le Gloahec and M. Koenig, *Physics of Plasmas* **16** (3), 033101 (2009).
- [11] K. Vaughan, A. S. Moore, V. Smalyuk, K. Wallace, D. Gate, S. G. Glendinning, S. McAlpin, H. S. Park, C. Sorce and R. M. Stevenson, *High Energy Density Physics* **9** (3), 635-641 (2013).
- [12] L. C. Jarrott, A. J. Kemp, L. Divol, D. Mariscal, B. Westover, C. McGuffey, F. N. Beg, M. Suggit, C. Chen, D. Hey, B. Maddox, J. Hawreliak, H. S. Park, B. Remington, M. S. Wei and A. MacPhee, *Physics of Plasmas* **21** (3), 031211 (2014).
- [13] A. Morace, L. Fedeli, D. Batani, S. Baton, F. N. Beg, S. Hulin, L. C. Jarrott, A. Margarit, M. Nakai, M. Nakatsutsumi, P. Nicolai, N. Piovella, M. S. Wei, X. Vaisseau, L. Volpe and J. J. Santos, *Physics of Plasmas* **21** (10), 102712 (2014).
- [14] E. Brambrink, S. Baton, M. Koenig, R. Yurchak, N. Bidaut, B. Albertazzi, J. E. Cross, G. Gregori, A. Rigby, E. Falize, A. Pelka, F. Kroll, S. Pikuz, Y. Sakawa, N. Ozaki, C. Kuranz, M. Manuel, C. Li, P. Tzeferacos and D. Lamb, *High Power Laser Science and Engineering* **4**, 101-105 (2016).
- [15] H. Sawada, S. Lee, T. Shioto, H. Nagatomo, Y. Arikawa, H. Nishimura, T. Ueda, K. Shigemori, A. Sunahara, N. Ohnishi, F. N. Beg, W. Theobald, F. Pérez, P. K. Patel and S. Fujioka, *Applied Physics Letters* **108** (25), 254101 (2016).
- [16] O. Klein and Y. Nishina, *Zeitschrift für Physik* **52** (11-12), 853-868 (2013).
- [17] R. Tommasini, C. Bailey, D. K. Bradley, M. Bowers, H. Chen, J. M. Di Nicola, P. Di Nicola, G. Gururangan, G. N. Hall, C. M. Hardy, D. Hargrove, M. Hermann, M. Hohenberger, J. P. Holder, W. Hsing, N. Izumi, D. Kalantar, S. Khan, J. Kroll, O. L. Landen, J. Lawson, D. Martinez, N. Masters, J. R. Nafziger, S. R. Nagel, A. Nikroo, J. Okui, D. Palmer, R. Sigurdsson, S. Vonnhof, R. J. Wallace and T. Zobrist, *Physics of Plasmas* **24** (5), 053104 (2017).
- [18] H. Chen, M. R. Hermann, D. H. Kalantar, D. A. Martinez, P. Di Nicola, R. Tommasini, O. L. Landen, D. Alessi, M. Bowers, D. Browning, G. Brunton, T. Budge, J. Crane, J. M. Di Nicola, T. Doppner, S. Dixit, G. Erbert, B. Fishler, J. Halpin, M. Hamamoto, J. Heebner, V. J. Hernandez, M. Hohenberger, D. Homoelle, J. Honig, W. Hsing, N. Izumi, S. Khan, K. LaFortune, J. Lawson, S. R. Nagel, R. A. Negres, L. Novikova, C. Orth, L. Pelz, M. Prantil, M. Rushford, M. Shaw, M. Sherlock, R. Sigurdsson, P. Wegner, C. Widmayer, G. J. Williams, W. Williams, P. Whitman and S. Yang, *Physics of Plasmas* **24** (3), 033112 (2017).
- [19] J. Myatt, W. Theobald, J. A. Delettrez, C. Stoeckl, M. Storm, T. C. Sangster, A. V. Maximov and R. W. Short, *Physics of Plasmas* **14** (5), 056301 (2007).
- [20] H. U. I. Chen and S. C. Wilks, *Laser and Particle Beams* **23** (4), 411-416 (2005).
- [21] S. Buffechoux, J. Psikal, M. Nakatsutsumi, L. Romagnani, A. Andreev, K. Zeil, M. Amin, P. Antici, T. Burris-Mog, A. Compant-La-Fontaine, E. d'Humieres, S. Fourmaux, S. Gaillard, F. Gobet, F. Hannachi, S. Kraft, A. Mancic, C. Plaisir, G. Sarri, M. Tarisien, T. Toncian, U. Schramm, M. Tampo, P. Audebert, O. Willi, T. E. Cowan, H. Pepin, V. Tikhonchuk, M. Borghesi and J. Fuchs, *Phys Rev Lett* **105** (1), 015005 (2010).
- [22] A. Compant La Fontaine, C. Courtois, E. Lefebvre, J. L. Bourgade, O. Landoas, K. Thorp and C. Stoeckl, *Physics of Plasmas* **20** (12), 123111 (2013).
- [23] M. Makita, G. Nersisyan, K. McKeever, T. Dzelzainis, S. White, B. Kettle, B. Dromey, D. Doria, M. Zepf, C. L. S. Lewis, A. P. L. Robinson, S. B. Hansen and D. Riley, *Physics of Plasmas* **21** (2), 023113 (2014).
- [24] A. J. Mackinnon, Y. Sentoku, P. K. Patel, D. W. Price, S. Hatchett, M. H. Key, C. Andersen, R. Snavely and R. R. Freeman, *Phys Rev Lett* **88** (21), 215006 (2002).

- [25] W. Theobald, K. Akli, R. Clarke, J. A. Delettrez, R. R. Freeman, S. Glenzer, J. Green, G. Gregori, R. Heathcote, N. Izumi, J. A. King, J. A. Koch, J. Kuba, K. Lancaster, A. J. MacKinnon, M. Key, C. Mileham, J. Myatt, D. Neely, P. A. Norreys, H. S. Park, J. Pasley, P. Patel, S. P. Regan, H. Sawada, R. Shepherd, R. Snavely, R. B. Stephens, C. Stoeckl, M. Storm, B. Zhang and T. C. Sangster, *Physics of Plasmas* **13** (4), 043102 (2006).
- [26] P. Neumayer, B. Aurand, M. Basko, B. Ecker, P. Gibbon, D. C. Hochhaus, A. Karmakar, E. Kazakov, T. Kuhl, C. Labaune, O. Rosmej, A. Tauschwitz, B. Zielbauer and D. Zimmer, *Physics of Plasmas* **17** (10), 103103 (2010).
- [27] M. N. Quinn, X. H. Yuan, X. X. Lin, D. C. Carroll, O. Tresca, R. J. Gray, M. Coury, C. Li, Y. T. Li, C. M. Brenner, A. P. L. Robinson, D. Neely, B. Zielbauer, B. Aurand, J. Fils, T. Kuehl and P. McKenna, *Plasma Physics and Controlled Fusion* **53** (2), 025007 (2011).
- [28] H. Sawada, M. S. Wei, S. Chawla, A. Morace, K. Akli, T. Yabuuchi, N. Nakanii, M. H. Key, P. K. Patel, A. J. Mackinnon, H. S. McLean, R. B. Stephens and F. N. Beg, *Phys Rev E Stat Nonlin Soft Matter Phys* **89** (3), 033105 (2014).
- [29] K. McKeever, M. Makita, G. Nersisyan, T. Dzelzainis, S. White, B. Kettle, B. Dromey, M. Zepf, G. Sarri, D. Doria, H. Ahmed, C. L. Lewis, D. Riley and A. P. Robinson, *Phys Rev E Stat Nonlin Soft Matter Phys* **91** (3), 033107 (2015).
- [30] S. R. Nagel, H. Chen, J. Park, M. Foord, A. U. Hazi, T. J. Hilsabeck, S. M. Kerr, E. V. Marley and G. J. Williams, *Applied Physics Letters* **110** (14), 144102 (2017).
- [31] S. Agostinelli, J. Allison, K. Amako, J. Apostolakis, H. Araujo, P. Arce, M. Asai, D. Axen, S. Banerjee, G. Barrand, F. Behner, L. Bellagamba, J. Boudreau, L. Broglia, A. Brunengo, H. Burkhardt, S. Chauvie, J. Chuma, R. Chytrcek, G. Cooperman, G. Cosmo, P. Degtyarenko, A. Dell'Acqua, G. Depaola, D. Dietrich, R. Enami, A. Feliciello, C. Ferguson, H. Fesefeldt, G. Folger, F. Foppiano, A. Forti, S. Garelli, S. Giani, R. Giannitrapani, D. Gibin, J. J. Gómez Cadenas, I. González, G. Gracia Abril, G. Greeniaus, W. Greiner, V. Grichine, A. Grossheim, S. Guatelli, P. Gumplinger, R. Hamatsu, K. Hashimoto, H. Hasui, A. Heikkinen, A. Howard, V. Ivanchenko, A. Johnson, F. W. Jones, J. Kallenbach, N. Kanaya, M. Kawabata, Y. Kawabata, M. Kawaguti, S. Kelner, P. Kent, A. Kimura, T. Kodama, R. Kokoulin, M. Kossov, H. Kurashige, E. Lamanna, T. Lampén, V. Lara, V. Lefebure, F. Lei, M. Liendl, W. Lockman, F. Longo, S. Magni, M. Maire, E. Medernach, K. Minamimoto, P. Mora de Freitas, Y. Morita, K. Murakami, M. Nagamatu, R. Nartallo, P. Nieminen, T. Nishimura, K. Ohtsubo, M. Okamura, S. O'Neale, Y. Oohata, K. Paech, J. Perl, A. Pfeiffer, M. G. Pia, F. Ranjard, A. Rybin, S. Sadilov, E. Di Salvo, G. Santin, T. Sasaki, N. Savvas, Y. Sawada, S. Scherer, S. Sei, V. Sirotenko, D. Smith, N. Starkov, H. Stoecker, J. Sulkimo, M. Takahata, S. Tanaka, E. Tcherniaev, E. Safai Tehrani, M. Tropeano, P. Truscott, H. Uno, L. Urban, P. Urban, M. Verderi, A. Walkden, W. Wander, H. Weber, J. P. Wellisch, T. Wenaus, D. C. Williams, D. Wright, T. Yamada, H. Yoshida and D. Zschiesche, *Nuclear Instruments and Methods in Physics Research Section A: Accelerators, Spectrometers, Detectors and Associated Equipment* **506** (3), 250-303 (2003).
- [32] S. M. Seltzer and M. J. Berger, *Nucl Instrum Meth B* **12** (1), 95-134 (1985).
- [33] S. M. Seltzer and M. J. Berger, *Atomic Data and Nuclear Data Tables* **35** (3), 345-418 (1986).
- [34] A. Miceli, R. Thierry, M. Bettuzzi, A. Flisch, J. Hofmann, U. Sennhauser and F. Casali, *Nuclear Instruments and Methods in Physics Research Section A: Accelerators, Spectrometers, Detectors and Associated Equipment* **580** (1), 123-126 (2007).
- [35] M. Guthoff, O. Brovchenko, W. de Boer, A. Dierlamm, T. Muller, A. Ritter, M. Schmanau and H. J. Simonis, *Nucl Instrum Meth A* **675**, 118-122 (2012).
- [36] M. Yucel, E. Emirhan, A. Bayrak, C. S. Ozben and E. B. Yucel, *Nucl Instrum Meth A* **799**, 50-53 (2015).
- [37] G. Malka and J. L. Miquel, *Phys Rev Lett* **77** (1), 75-78 (1996).
- [38] H. Schwoerer, P. Gibbon, S. Dusterer, R. Behrens, C. Ziener, C. Reich and R. Sauerbrey, *Phys Rev Lett* **86** (11), 2317-2320 (2001).

-
- [39] G. Malka, M. M. Aleonard, J. F. Chemin, G. Claverie, M. R. Harston, J. N. Scheurer, V. Tikhonchuk, S. Fritzler, V. Malka, P. Balcou, G. Grillon, S. Moustazis, L. Notebaert, E. Lefebvre and N. Cochet, *Phys Rev E Stat Nonlin Soft Matter Phys* **66** (6 Pt 2), 066402 (2002).
- [40] A. G. Mordovanakis, P. E. Masson-Laborde, J. Easter, K. Popov, B. X. Hou, G. Mourou, W. Rozmus, M. G. Haines, J. Nees and K. Krushelnick, *Applied Physics Letters* **96** (7), 071109 (2010).
- [41] T. Yabuuchi, K. Adumi, H. Habara, R. Kodama, K. Kondo, T. Tanimoto, K. A. Tanaka, Y. Sentoku, T. Matsuoka, Z. L. Chen, M. Tampo, A. L. Lei and K. Mima, *Physics of Plasmas* **14** (4), 040706 (2007).
- [42] T. Tanimoto, H. Habara, R. Kodama, M. Nakatsutsumi, K. A. Tanaka, K. L. Lancaster, J. S. Green, R. H. H. Scott, M. Sherlock, P. A. Norreys, R. G. Evans, M. G. Haines, S. Kar, M. Zepf, J. King, T. Ma, M. S. Wei, T. Yabuuchi, F. N. Beg, M. H. Key, P. Nilson, R. B. Stephens, H. Azechi, K. Nagai, T. Norimatsu, K. Takeda, J. Valente and J. R. Davies, *Physics of Plasmas* **16** (6), 062703 (2009).
- [43] Y. Sentoku and A. J. Kemp, *Journal of Computational Physics* **227** (14), 6846-6861 (2008).
- [44] F. N. Beg, A. R. Bell, A. E. Dangor, C. N. Danson, A. P. Fews, M. E. Glinsky, B. A. Hammel, P. Lee, P. A. Norreys and M. Tatarakis, *Physics of Plasmas* **4** (2), 447-457 (1997).
- [45] H. W. Koch and J. W. Motz, *Rev Mod Phys* **31** (4), 920-955 (1959).
- [46] Y. Glinec, J. Faure, L. L. Dain, S. Darbon, T. Hosokai, J. J. Santos, E. Lefebvre, J. P. Rousseau, F. Burgy, B. Mercier and V. Malka, *Phys Rev Lett* **94** (2), 025003 (2005).
- [47] C. Courtois, R. Edwards, A. C. La Fontaine, C. Aedy, M. Barbotin, S. Bazzoli, L. Biddle, D. Brebion, J. L. Bourgade, D. Drew, M. Fox, M. Gardner, J. Gazave, J. M. Lagrange, O. Landoas, L. Le Dain, E. Lefebvre, D. Mastrosimone, N. Pichoff, G. Pien, M. Ramsay, A. Simons, N. Sircombe, C. Stoeckl and K. Thorp, *Physics of Plasmas* **18** (2), 023101 (2011).
- [48] C. Courtois, R. Edwards, A. C. La Fontaine, C. Aedy, S. Bazzoli, J. L. Bourgade, J. Gazave, J. M. Lagrange, O. Landoas, L. Le Dain, D. Mastrosimone, N. Pichoff, G. Pien and C. Stoeckl, *Physics of Plasmas* **20** (8), 083114 (2013).
- [49] Y. Ping, R. Shepherd, B. F. Lasinski, M. Tabak, H. Chen, H. K. Chung, K. B. Fournier, S. B. Hansen, A. Kemp, D. A. Liedahl, K. Widmann, S. C. Wilks, W. Rozmus and M. Sherlock, *Phys Rev Lett* **100** (8), 085004 (2008).
- [50] L. G. Huang, H. P. Schlenvoigt, H. Takabe and T. E. Cowan, *Physics of Plasmas* **24** (10), 103115 (2017).
- [51] S. C. Wilks, W. L. Kruer, M. Tabak and A. B. Langdon, *Phys Rev Lett* **69** (9), 1383-1386 (1992).
- [52] M. J. Berger, J. Coursey, M. Zucker and J. Chang, *Stopping-power and range tables for electrons, protons, and helium ions*. (NIST Physics Laboratory Gaithersburg, MD, 1998).